Meas. Sci. Technol. **19** (2008) 065402 (13pp) doi:10.1088/0957-0233/19/6/065402

An improved three-dimensional characterization of defocusing digital particle image velocimetry (DDPIV) based on a new imaging volume definition

R L Grothe and D Dabiri

Department of Aeronautics and Astronautics, University of Washington, Seattle, WA, USA

Received 4 February 2008, in final form 29 February 2008
Published 29 April 2008
Online at stacks.iop.org/MST/19/065402

Abstract

The full development of the equations for defocused digital particle image velocimetry as proposed by Kajitani and Dabiri (2005 *Meas. Sci. Technol.* **16** 790–804) predefined a finite area at the focal plane to be imaged onto the CCDs. This resulted in bounded overlapping viewing cones of the lenses, i.e. the observable domain, within which a tetrahedral imaging volume was defined. The resulting ray tracing suggested that the observable domain would not be fully imaged onto the CCDs. Furthermore, the tetrahedral imaging volume, which was also a definition used to develop the characteristic three-dimensional DDPIV equations, only represented a limited portion of the observable domain. It is shown that by avoiding these incorrect definitions, a more accurate description of the three-dimensional DDPIV measurement system can be developed by introducing a new measurement volume based on the CCD dimensions, which replaces the tetrahedral volume, as well as introducing a new system optical axis. Lastly, a geometric uncertainty analysis is conducted and compared to the results found by Kajitani and Dabiri.

Keywords: defocusing digital particle image velocimetry, DDPIV, cross-correlation analysis, velocimetry, imaging, visualization, fluid flow, fluid diagnostics

(Some figures in this article are in colour only in the electronic version)

Nomenclature

γ	radial distance from the optical axis to the lens axes
ζ	distance from an equilateral triangle's centroid to any one of its vertices
a_{pf}	triangle side-length of the front face of the volume of interest in the present derivation
a_{pb}	triangle side-length of the rear face of the volume of interest in the present derivation
a_{pfx}	rectangle width of the front face of the volume of interest in the present derivation
a_{pfy}	rectangle height of the front face of the volume of interest in the present derivation
a_{pbx}	rectangle width of the rear face of the volume of interest in the present derivation
a_{pby}	rectangle height of the rear face of the volume of interest in the present derivation
a_z	thickness of the volume of interest in the present derivation
b	particle image separation
d	equilateral triangle side-length distance between the lenses
d_{cw}	distance from the lens plane to the test section wall
f	focal length of the lenses
H	the height at the focal plane within the observable domain at the reference distance, L_{ft}
h_1	CCD width
h_2	CCD height
L_{apft}	location of the front face of the domain of interest relative to the lens plane
L_p	distance from the lenses to the CCD sensors along the optical axis
L_{ft}	distance from the lens to the focal plane along the optical axis

M optical magnification
X X-coordinate of a particle in the global coordinate system
x_0 x-coordinate of an equilateral triangle's centroid mapped by the triple CCDs' exposure of a particle in the local CCD coordinate system
x_b x-coordinate of the bottom vertex of the image in the local CCD coordinate system
x_{ccd} x-coordinate of the center of the CCD measured from the system optical axis
x_{tl} x-coordinate of the top-left vertex of the image in the local CCD coordinate system
x_{tr} x-coordinate of the top-right vertex of the image in the local CCD coordinate system
Y Y-coordinate of a particle in the global coordinate system
y_0 y-coordinate of an equilateral triangle's centroid mapped by the triple CCDs' exposure of a particle in the local CCD coordinate system
y_b y-coordinate of the base vertex of the image in the local coordinate system
y_{ccd} y-coordinate of the center of the CCD measured from the system optical axis
y_{tl} y-coordinate of the top-left vertex of the image in the local CCD coordinate system
y_{tr} y-coordinate of the top-right vertex of the image in the local CCD coordinate system
Z Z-coordinate of a particle in the global coordinate system
$Z_{\min}$ location of the intersection of the emerging rays from the lenses on the optical axis

1. Introduction

PIV techniques have become more prevalent as a means to interrogate and study fluid flows. Many of the three-dimensional flows, however, cannot be fully understood by interrogating them with two-dimensional PIV techniques, so having the ability to capture three-component velocities within a three-dimensional volume is necessary. Towards this end, 3D digital particle tracking velocimetry (3DDPTV) (Maas *et al* 1993, Murai *et al* 1980, Virant and Dracos 1997) has been developed, in which individual particles are tracked in time in a Lagrangian sense using multiple cameras arranged to have differing perspectives of the same volume in space. Holographic particle image velocimetry (HPIV) (Barnheart *et al* 1994, Zimin *et al* 1993, Meng and Hussain 1995, Zhang *et al* 1997) has also been developed, which is capable of providing high resolution spatial data at one instant in time by recording the flow onto a hologram. Though these methods are useful in their own right, there are also certain drawbacks of each. 3DDPTV, for example, requires time-consuming calibration for each camera. Also, low particle densities result in low spatial resolution, and high densities result in triangulation failures, due to improper particle differentiation, which result in incorrect particle tracking. HPIV, on the other hand, is extremely accurate, using 2D slices from the holographic image to reconstruct 3D velocity vectors. However, its setup is very sensitive to slight environmental disturbances, it is time consuming to implement and it can only provide a velocity field at a single point in time.

Another three-dimensional volumetric velocity measurement technique, defocusing digital particle image velocimetry (DDPIV), was introduced by Willert and Gharib (1992). The mathematical equations behind this method were mainly established by Pereira *et al* (2000) and further elaborated on by Pereira and Gharib (2002) (henceforth PG). Whereas these equations were appropriate only for a two-dimensional optical arrangement, Kajitani and Dabiri (2005) (henceforth KD, see also Kajitani and Dabiri (2008)) developed the mathematical equations appropriate for a fully three-dimensional optical arrangement, where a finite viewing area at the focal plane was predefined. However, these latter equations were derived considering a tetrahedral imaging volume defined by inscribing an equilateral triangle into the overlapping viewing cones, i.e. the observable domain, for each lens. In these derivations, the viewing cones were assumed to be bound by the geometric imaging of a finite area at the focal plane onto the CCDs. This resulted in an observable domain that was not fully imaged onto the CCDs. The purpose of this paper is to therefore remove this predefinition, and show that a more correct imaging volume definition is the one that matches the shape of the CCDs, thereby avoiding the use of the tetrahedral volume defined by KD. Towards this end, section 2 will review the imaging volume definition in KD and discuss its limitations; section 3 will introduce the new imaging volume definition and a new optical axis for the system; section 4 will present the geometric uncertainty analysis; and section 5 will present the conclusions.

2. Previous imaging volume definition

In Pereira *et al* and PG, a cubic imaging volume was inscribed inside the true observable domain. For the purpose of analysis, KD later defined a tetrahedral imaging volume that represented the domain observable to all lenses, shown in figure 1. In this figure, the cones of vision image the finite circular area common to all lenses at the focal plane, towards the left of the figure onto the CCDs on the right side of the figure. The inset plane cut view in figure 1 shows the inscribed equilateral triangle cross-section from the tetrahedral imaging volume within the observable overlapped region.

Since the area at the focal plane was predefined in KD, the bounding viewing cones imaging this area onto the CCDs resulted in the ray tracing shown in figures 2 and 3, identifying KD's definition for the imaging volume with the dimensions labeled. For clarity, figure 4 shows a three-dimensional view of this imaging volume proposed by KD. Figure 5 shows the limits of the projection of this tetrahedral imaging volume onto three CCDs (the left showing rectangular CCDs and the right showing square CCDs), placed such that the equilateral triangle from the volume just fills the width of the CCDs. First, to fully image the triangular region, a virtual CCD must be used, which will be slightly rectangular, shown by the solid line in figure 5. Second, given this arrangement proposed by KD,

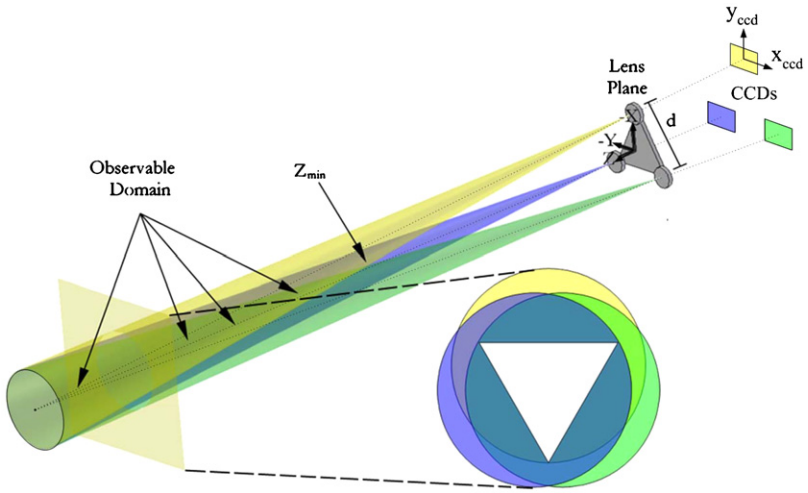

Figure 1. Cones of vision formed by lenses placed at the vertices of an equilateral triangle with the overlapped region shown in blue and the inscribed white imaging volume shape. Note the discrepancy between coordinate systems for the lenses and the CCDs (adapted from KD).

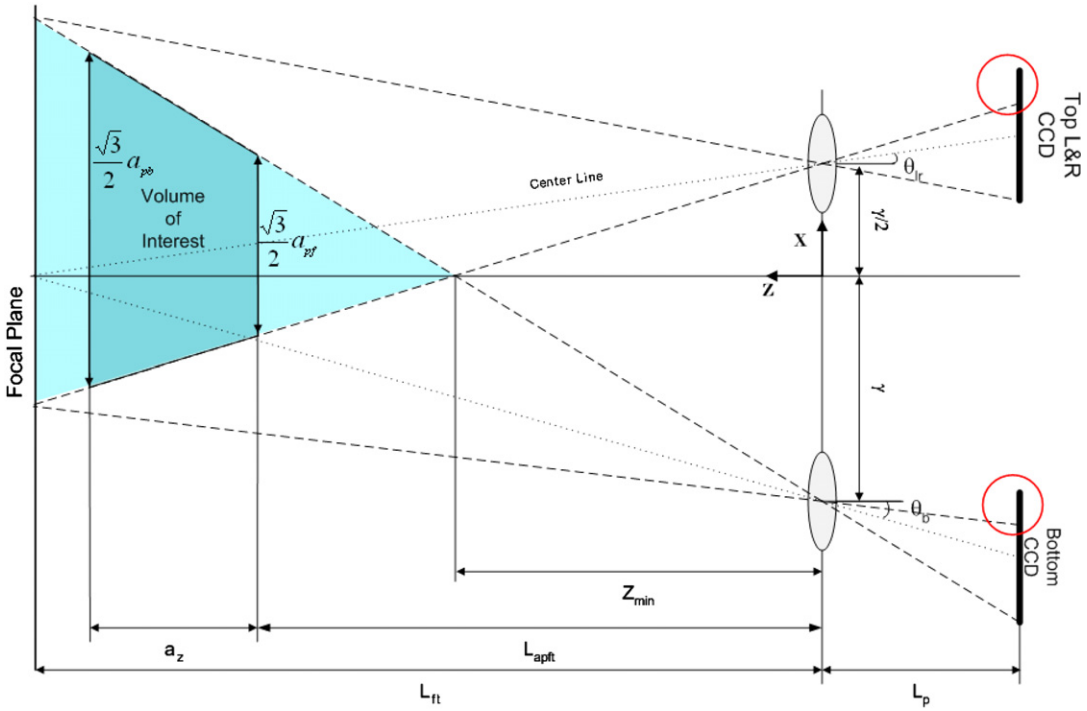

Figure 2. Tetrahedral imaging volume defined in the *X*–*Z* plane with virtual CCDs. Regions of unused CCD are indicated by the red circles. The volume of interest is shown by the dark blue region, while the observable domain is identified by the combined light and dark blue region.

figures 2, 3 and 5 show that the centroid of the CCDs should be coincident with the centroid of the equilateral triangle. The effect of this can be seen in the upper right portion of figure 2 for the top-left and right CCDs in the enclosed circles; the entire virtual CCD is not being utilized to define the volume. This is easier to see in figure 5(*a*), where the equilateral triangle does not completely fill the CCDs' area. Should the CCD be square, figure 5(*b*) also shows that the entire CCD is still not being utilized by the defined volume. For rectangular CCDs, KD projected the triple exposure (triplet) of the imaged particle at $Z_{\min}$ onto the CCD such that its horizontal side length filled the horizontal dimension of the CCD as shown in figure 5(*a*).

To understand the effects of such limitations on the imaging volume, the CCD images shown in figure 5 are back-projected into the imaging volume, and are presented in figure 6, where a planar cut of the imaging volume at L_{apft} is shown on the left, while the right image shows a planar cut at $a_z + L_{apft}$ (see also figure 3). Note that the image becomes inverted from the triangular arrangement of the lenses shown in figure 5, since the imaging volume is on the opposite side of the lenses. The dashed lines refer to what is imaged by an actual

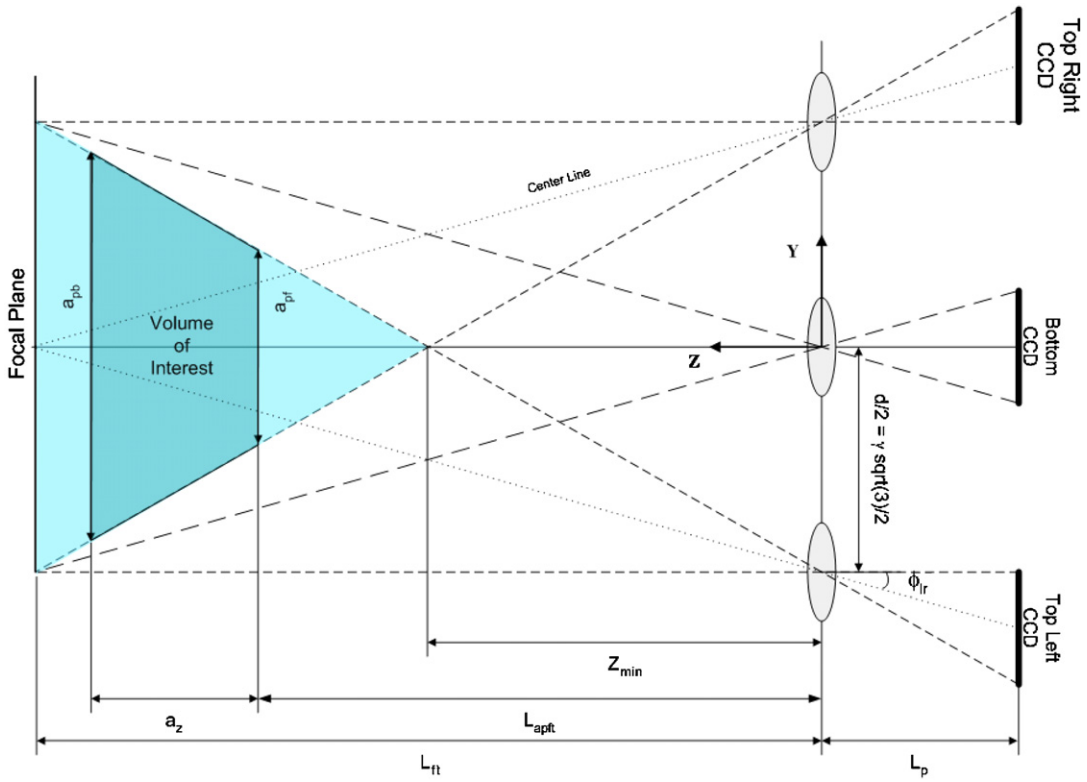

Figure 3. Tetrahedral imaging volume defined in the *Y–Z* plane with virtual CCDs. The volume of interest is shown by the dark blue region, while the observable domain is identified by the combined light and dark blue region.

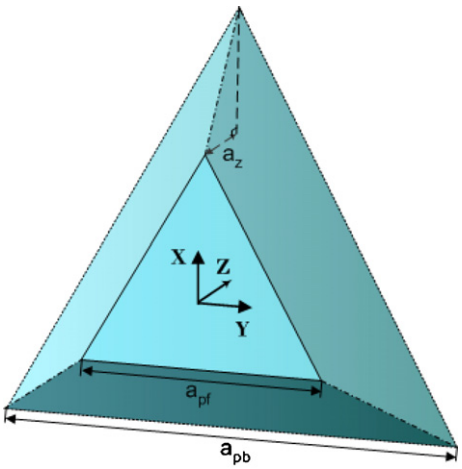

Figure 4. Three-dimensional view of the tetrahedral imaging volume.

rectangular CCD, while the solid rectangles with inscribed equilateral triangles match the definition for the virtual CCD given in figure 5. By definition, on the focal plane, these three would perfectly overlap. The choices for the cut locations are made to illustrate the extremes of the imaging volume: even though the side length of the equilateral triangle making up the front face of the imaging volume is still relatively large, the definition of the imaging volume limits the amount of the overlapped triangles actually visible by all three CCDs (shown within the blue box) as shown by the small portion of the solid white region within the blue box on the left image. Closer to the focal plane, shown in figure 6 right, this becomes less of an issue as the area of the overlapped triangles increases within the overlapping CCDs (also shown by the blue box). These limitations are a consequence of predefining a finite area at the focal length to be imaged onto the CCDs, which shall be addressed below, in section 3.

3. New imaging volume definition

In reality, predefining a finite area at the focal plane does not bound the cones of vision of the lenses nor what is imaged onto the CCDs. Rather, since the cones of vision create a much wider imaging cone, the CCDs determine the area that is imaged at the focal plane. Consequently, it will be possible to define a more useful imaging volume based entirely upon the CCD dimensions, which will therefore better describe what is observed when using a DDPIV system. Furthermore, due to the inclusion of the CCDs in the DDPIV description, the optical coordinate system and the CCDs' image coordinate system should be consistent. Figure 1, however, shows the conflict between these sets of axes; as a result, a redefinition of the optical system coordinates is made from x to $-y$ and y to x. Maintaining the same optical arrangement as set forth by KD (lenses arranged in an equilateral triangle), and

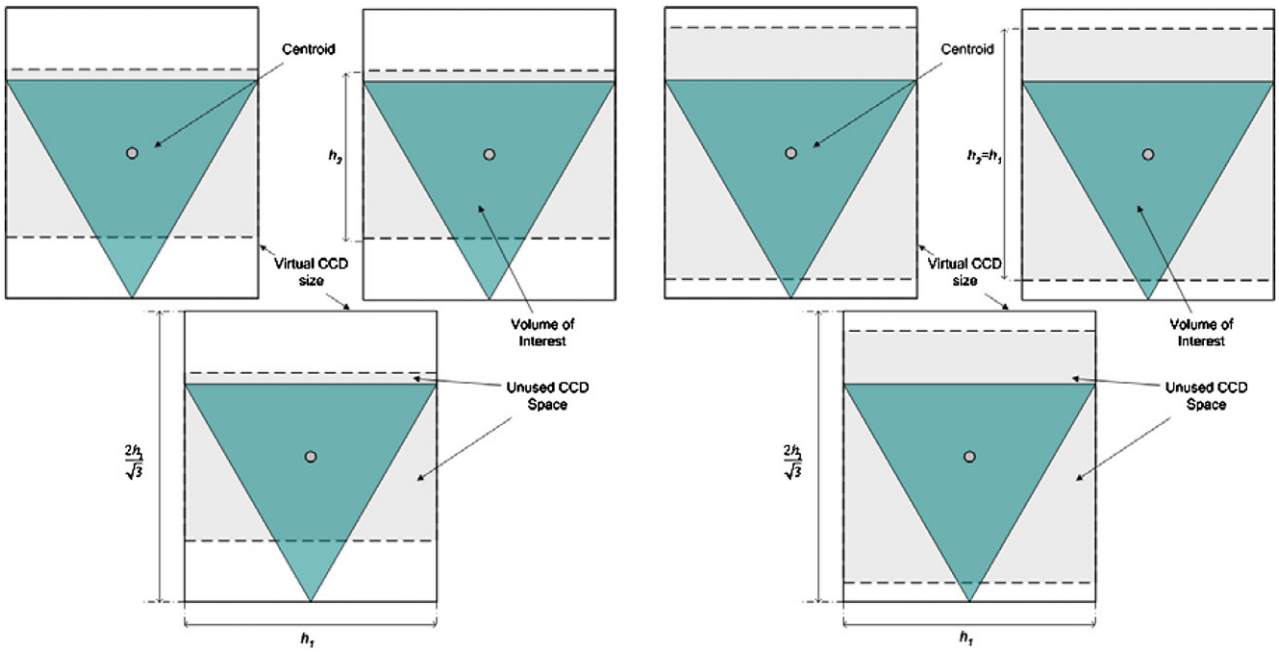

Figure 5. Definition of imaging volume projected onto upper left, upper right and bottom CCDs for (*a*) rectangular CCDs and (*b*) square CCDs.

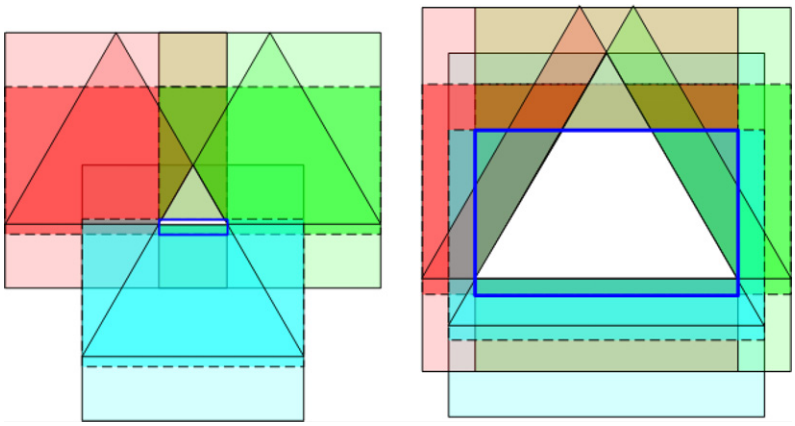

Figure 6. Relative size of the volume of interest (indicated by the solid white) using the equilateral triangle definition shown in figure 5, at $Z = L_{apft}$ (left) and $Z = a_z + L_{apft}$ (right).

using rectangular CCDs, the resulting new geometric setup and distance definitions are shown in figures 11 and 12. Note that in comparison to figure 5, this ray tracing correctly allows for the full exposure of the CCDs. Furthermore, by placing the system optical axis (z-axis) at the half-height and half-width of the lens' triangular shape (see figures 2, 3 and 10), an imaging volume can be obtained that is rectangular and symmetric, as shown in figure 7. It should be pointed out that a rectangular volume can also be defined with the system optical axis located at the centroid of the lenses, as in KD. However, this would result in an imaging volume that would be asymmetric about the optical axis (see figure 8), with its coordinate system located at $1/3$ and $1/2$ of the imaging volume's respective dimensions in the y- and x-planes.

The fully exposed CCD images, when back-projected into the imaging volume, are presented in figure 9, where a planar cut of the imaging volume at L_{apft} is shown on the left, while the right image shows a planar cut at $a_z + L_{apft}$ (see also figure 8). The limits of this new volumetric region are defined by the upper outside right and left corners of the top-left and top-right CCDs, respectively, and the bottom edge of the lower CCD identified by its midpoint, marked in figure 9 as red, green and blue circles, respectively, which correspond to the limits of view of the CCDs. Note again that the imaged area becomes inverted from that of the lens arrangement because of the crossing at the lens plane. In addition, figures 7 and 9 also illustrate the improvements of this method over that of the tetrahedral volume, since the new imaging volume

Table 1. Comparison between sensor particle location equations in KD and present derivation.

	KD	Present derivation	Equation
x_{tl}	$\frac{M}{2Z}[-d(L_{ft}-Z)-2L_{ft}X]$	$\frac{M}{2Z}[-d(L_{ft}-Z)-2L_{ft}X]$	(1)
x_{tr}	$\frac{M}{2Z}[d(L_{ft}-Z)-2L_{ft}X]$	$\frac{M}{2Z}[d(L_{ft}-Z)-2L_{ft}X]$	(2)
x_b	$-\frac{ML_{ft}X}{Z}$	$-\frac{ML_{ft}X}{Z}$	(3)
$y_{tl},\ y_{tr}$	$-\frac{M}{2Z}\left[2L_{ft}Y+\frac{d}{\sqrt{3}}(L_{ft}-Z)\right]+\frac{2-\sqrt{3}}{2\sqrt{3}}h_1$	$-\frac{M}{Z}\left(L_{ft}Y+\frac{\sqrt{3}}{4}d(L_{ft}-Z)\right)$	(4)
y_b	$-\frac{M}{Z}\left[L_{ft}Y-\frac{d}{\sqrt{3}}(L_{ft}-Z)\right]+\frac{2-\sqrt{3}}{2\sqrt{3}}h_1$	$-\frac{M}{Z}\left(L_{ft}Y-\frac{\sqrt{3}}{4}d(L_{ft}-Z)\right)$	(5)

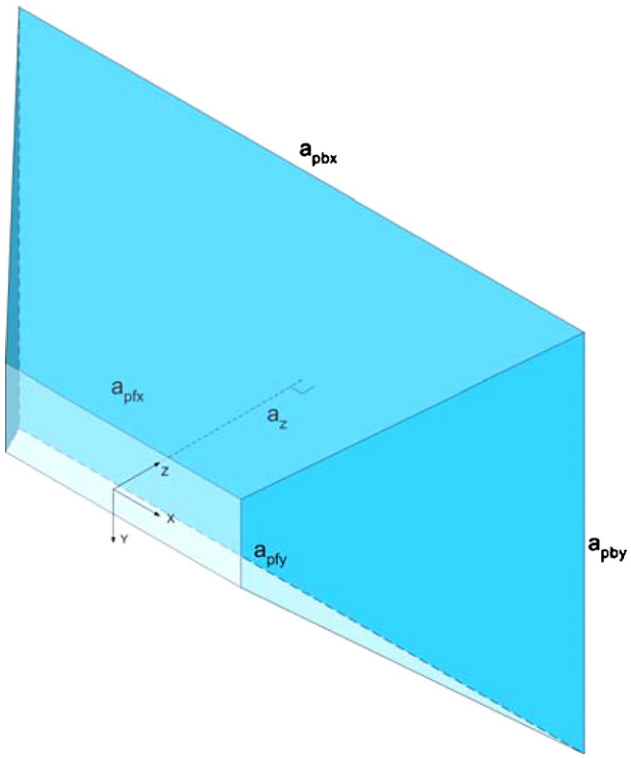

Figure 7. Three-dimensional view of the rectangular imaging volume.

definition allows for full CCD utilization in this improved DDPIV characterization.

Given this new geometric arrangement, the modified relations expressing the particle locations on the CCDs with respect to KD are shown in table 1, where L_{ft} is the distance to the focal plane, Z is the particle's physical depth location found using the equations from KD, M is the optical magnification, the small x and y indicate pixel locations of an imaged particle on the CCD and the subscripts *tl*, *tr* and *b* indicate top-left, top-right and bottom respectively, from the camera perspective. Inverting and simplifying equations (1)–(5) result in the relations for the location of particles in physical space, as shown in table 2. The KD equations in this table have been slightly modified from their original form such that the coordinate systems and naming conventions match those defined for the new geometric arrangement. Note again that in this case, there is no arbitrary and artificial cross-sectional shape imposed on the imaging volume but rather it is naturally derived from the shape of the CCD, allowing for accurate

Table 2. Comparison between CCD particle location equations in KD and present derivation.

	KD	Present derivation	Equation
X	$\frac{-x_0 Z}{L_{ft}M}$	$\frac{-x_0 Z}{L_{ft}M}$	(6*a*)
x_0	$\frac{x_{tl}+x_{tr}+x_b}{3}$	$\frac{x_{tl}+x_{tr}+x_b}{3}$	(6*b*)
Y	$\frac{-y_0 Z}{L_{ft}M}$	$\frac{-y_0 Z}{L_{ft}M}$	(7*a*)
y_0	$\frac{(y_{tl}+y_{tr}+y_b)}{3}$	$\frac{[(y_{tl}+y_{tr})/2]+y_b}{2}$	(7*b*)
Z	$Z=\left(\frac{1}{L_{ft}}+\frac{b}{MdL_{ft}}\right)^{-1}$ $=\left(\frac{1}{L_{ft}}+\frac{\zeta}{M\gamma L_{ft}}\right)^{-1}$	$Z=\left(\frac{1}{L_{ft}}+\frac{b}{MdL_{ft}}\right)^{-1}$	(8)

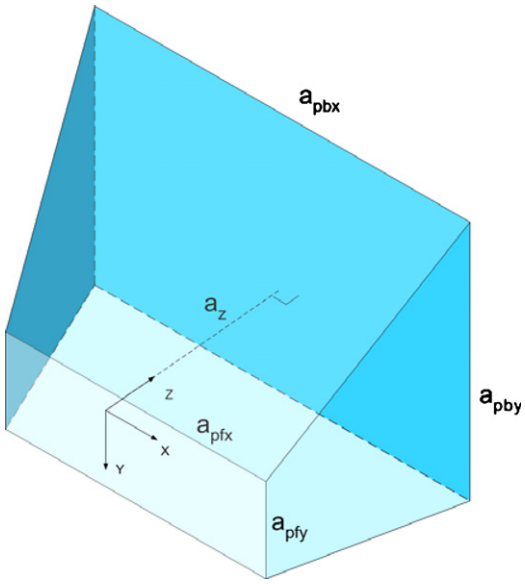

Figure 8. Skewed rectangular imaging volume.

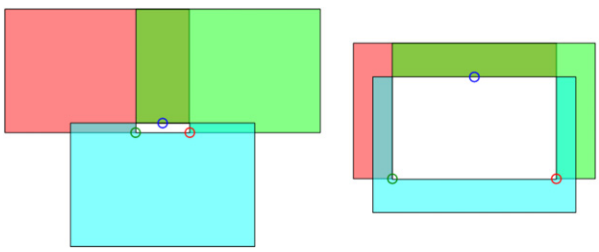

Figure 9. Relative size of the volume of interest (indicated by the solid white) using the rectangular definition at $Z = L_{apft}$ (left) and $Z = a_z + L_{apft}$ (right), with the circles indicating the respective points used to define the extents of the imaging volume.

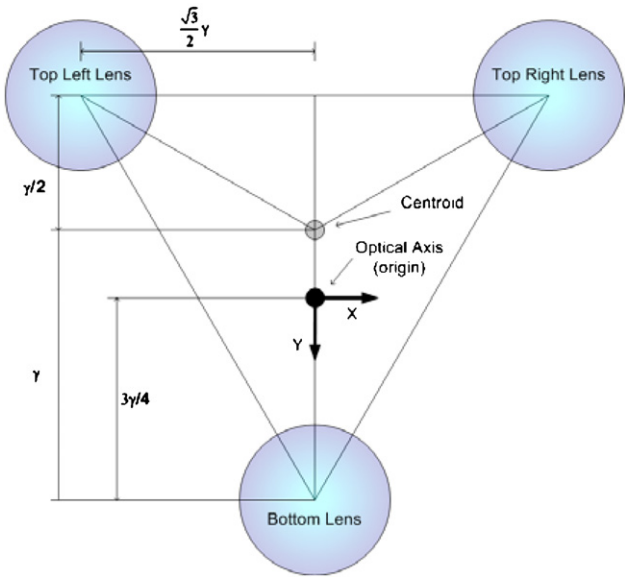

Figure 10. Lens dimensions for a rectangular imaging volume.

full utilization of the available CCD space. Additionally, unlike KD where the radial distance from the centroid of an imaged equilateral triangle, ζ, was the more natural triplet size measure, for both the rectangular and square CCD cases, it is now more convenient to use b, the triplet side-length, as it can be seen from figure 10 that ζ is no longer intrinsically defined from the new system optical axis.

For the X-direction equations, the present derivation and KD are the same because in that plane, the systems are arranged symmetrically. The biggest changes occur in the Y-direction equations because in the present derivation the equations for the top two CCDs as well as the bottom CCD are symmetric about the newly defined optical axis, where the only difference is in the signs of the second terms of equations (4) and (5). In KD, these equations differed from each other because there is no symmetry about the optical x- and y-axes. A similar change is noted in the equations for finding the physical particle location in table 2 as for those given in table 1. Only the equation for the Y-direction is different in the present derivation, because the optical axis has been shifted to give a symmetric rectangular region about the origin. For this reason, y_0 is shifted to the half-height of the imaged triplet as opposed to the centroid as given in KD.

While the present discussions have focused on the use of rectangular CCDs, they are also applicable to square CCDs. An example is shown in figure 13 of planar cuts of the imaging volume described by a square CCD, as well as its three-dimensional view (see figure 14). Like the rectangular CCDs, it can be seen that the imaging volume of the CCDs continues to separate from one another in an equilateral fashion, leading to a vertically elongated rectangular front face for the imaging volume and a slightly off-square cross-section near the back of the volume. Note, that at the focal plane, the imaging volume would again be square and completely overlapped, as by design.

Table 3. Comparison between optical setup equations in KD and present derivation for a rectangular CCD with its shorter dimension aligned in the y-axis.

	KD	Present derivation	Equation
$Z_{\min}$	$L_{apft} - a_z\left(\frac{a_{pf}}{a_{pb}-a_{pf}}\right)$	$L_{apft} - a_z\left(\frac{a_{pfy}}{a_{pby}-a_{pfy}}\right)$	(9)
d	$\frac{L_{apft}(a_{pb}-a_{pf})}{a_z} - a_{pf}$	$\frac{2}{\sqrt{3}}\left(\frac{L_{apft}(a_{pby}-a_{pfy})}{a_z} - a_{pfy}\right)$	(10)

Table 4. Comparison between optical setup equations in KD and present derivation for a rectangular CCD with its shorter dimension aligned in the x-axis.

	KD	Present derivation	Equation
$Z_{\min}$	$L_{apft} - a_z\left(\frac{a_{pf}}{a_{pb}-a_{pf}}\right)$	$L_{apft} - a_z\left(\frac{a_{pfx}}{a_{pbx}-a_{pfx}}\right)$	(11)
D	$\frac{L_{apft}(a_{pb}-a_{pf})}{a_z} - a_{pf}$	$\frac{L_{apft}(a_{pbx}-a_{pfx})}{a_z} - a_{pfx}$	(12)

Modifications are also necessary to the equations for $Z_{\min}$, the minimum distance from the lens plane that can be imaged on all three CCDs, and d, the lens separation. In KD, these were shown to be functions of a_{pf} and a_{pb} (see figure 7), since their imaging volume was characterized by an equilateral triangle with the side length of the equilateral triangle as its characteristic length. However, the new imaging volume is a rectangle with two characteristic lengths, so the previous imaging volume dimensions a_{pf} and a_{pb} need to be replaced with a_{pfx}, a_{pfy}, a_{pbx} and a_{pby}. Using similar triangles (see figures 11 and 12), the modified equations in comparison with KD are shown in table 3, where L_{apft} is the distance from the lens plane to the front of the imaging volume and a_z is the depth of the imaging volume, as shown previously. The main difference is that now, out of two sets of characteristic lengths for the imaging volume, the one that diminishes most quickly must be correctly chosen for use in determining $Z_{\min}$ and d. The correct dimension to use is denoted by the subscript appended to a_{pb} and a_{pf}.

With a rectangular CCD, the shorter dimension should be aligned with the y-axis because this is the dimension in which overlap will diminish first, thus defining $Z_{\min}$. If the shorter dimension was instead aligned with the x-axis or if the CCD is square (see figure 13), a_{pfy} and a_{pby} in equations (9) and (10) are replaced with a_{pfx} and a_{pbx}, respectively, and the $\frac{2}{\sqrt{3}}$ pre-multiplier in equation (10) can be removed (see equations (11) and (12) in table 4).

The remaining equations for the DDPIV system remain unchanged from KD. It is, however, important to consider the constraints on the CCD placement, namely defining the outer limits of the imaging volume, as discussed above, and centering on the system's optical axis at the focal plane (see figures 11 and 12). In KD, assumptions were used in restricting the lens' viewing cones, thereby restricting the description of the observable domain. But to fully define the imaging volume, the CCD locations must be determined. This can be done using the similar triangle relations given in equations (13) and (14) along with the standard thin-lens equation solved for L_p in equation (15):

$$\frac{L_{ft}}{\frac{\sqrt{3}}{4}d} = \frac{L_p}{y - \frac{\sqrt{3}}{4}d} \tag{13}$$

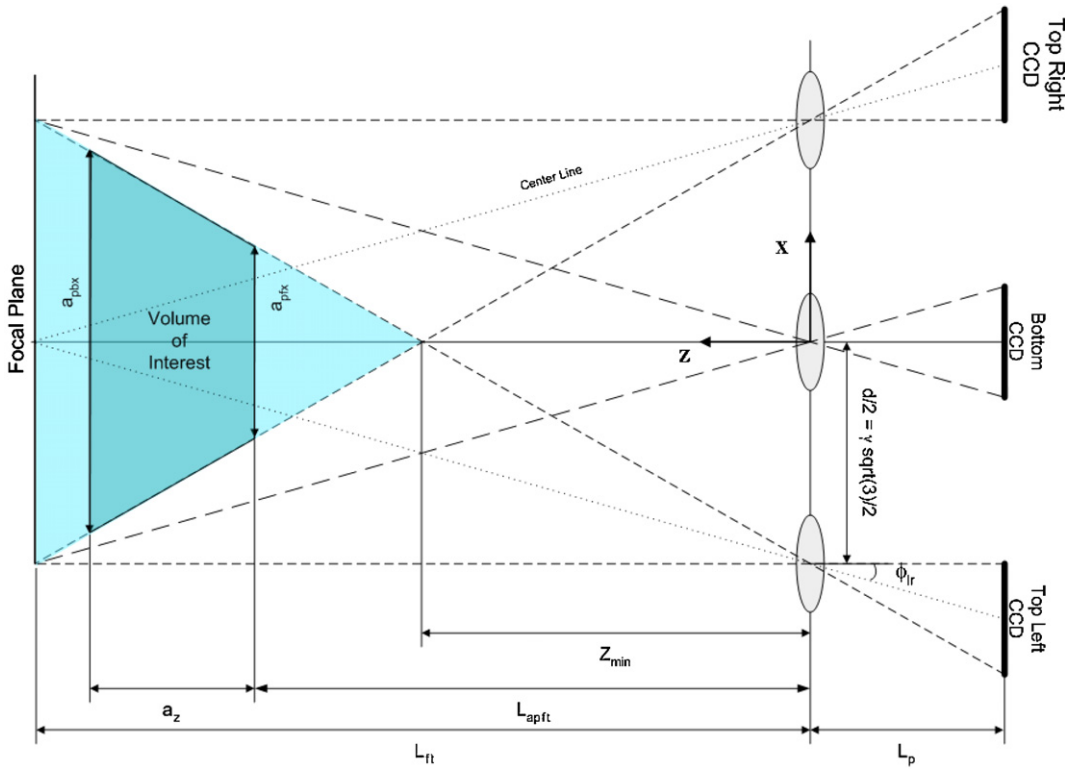

Figure 11. Rectangular imaging volume defined in the *X*–*Z* plane. The volume of interest is shown by the dark blue region, while the observable domain is identified by the combined light and dark blue region.

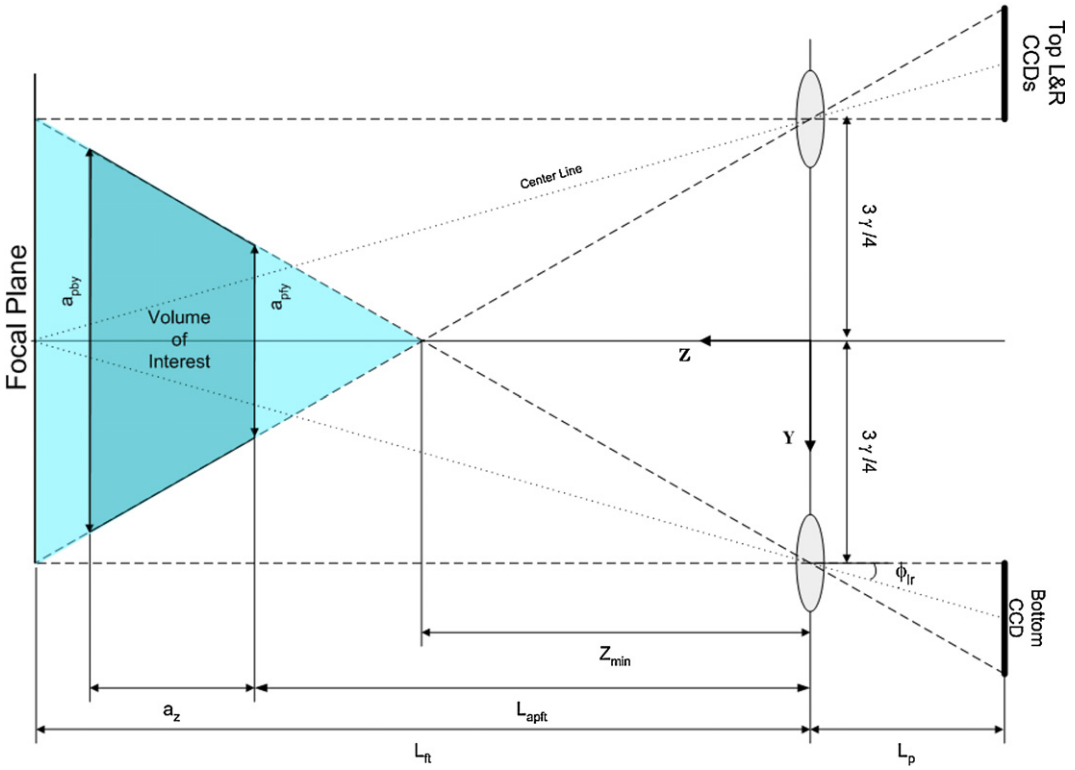

Figure 12. Rectangular imaging volume defined in the *Y*–*Z* plane. The volume of interest is shown by the dark blue region, while the observable domain is identified by the combined light and dark blue region.

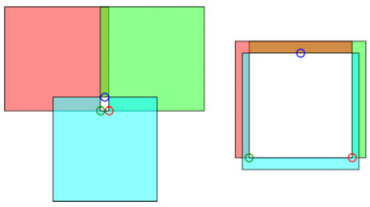

Figure 13. Relative size of the volume of interest (indicated by the solid white) using square CCDs cut at $Z = L_{apft}$ (left) and $Z = a_z + L_{apft}$ (right), with the red circles indicating the points used to define the imaging volume extents.

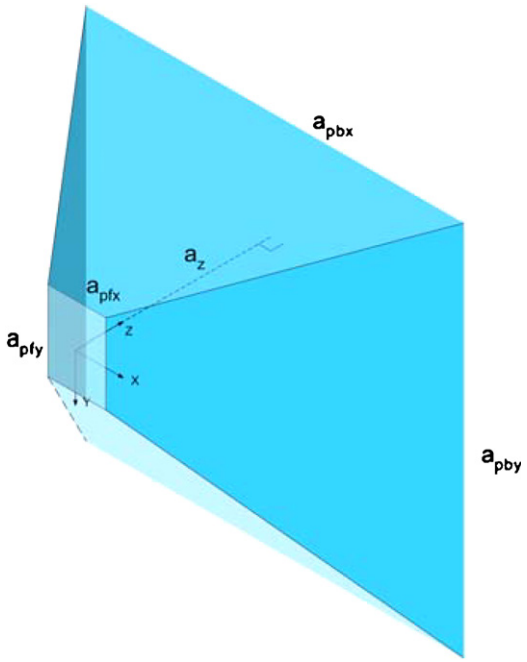

Figure 14. Three-dimensional view of the square imaging volume.

$$\frac{y + \frac{h_2}{2}}{L_p + Z_{\min}} = \frac{\frac{\sqrt{3}}{4}d}{Z_{\min}} \tag{14}$$

$$L_p = \frac{f \cdot L_{ft}}{L_{ft} - f}. \tag{15}$$

Combining these constraining equations for centering and the outer viewing limits with the physical dimensions of the CCDs results in a set of equations that fully constrain the CCDs. Equation (16) identifies the CCD location in the Z-direction with respect to the lens plane (L_p); equation (17) identifies the focal plane of the system in the Z-direction with respect to the lens plane (L_{ft}), and equation (18) sets the magnitude of the vertical displacement from the system's optical axis for the center of all three CCDs (y_{ccd})—the bottom is displaced in the positive y-direction and the top-left and top-right are displaced in the negative y-direction. The magnitude of the horizontal displacement for the center of the top-left and top-right CCDs (x_{ccd}) is given in equation (19) (the bottom CCD has no displacement in the x-direction). The reason there needs only be one equation for each of the x- and y-directions is that the new imaging volume definition places the CCDs symmetrically about the system optical axis in both directions, whereas in KD, there would need to be two different equations for the y-direction displacements above and below the system optical axis.

$$L_p = \frac{\left(\frac{2}{3}\sqrt{3}h_2 - d\right)Z_{\min} f}{d(f - Z_{\min})} \tag{16}$$

$$L_{ft} = \frac{(\sqrt{3}d - 2h_2)Z_{\min} f}{\sqrt{3}df - 2h_2 Z_{\min}} = \frac{f \cdot L_p}{L_p - f} \tag{17}$$

$$y_{\text{CCD}} = \frac{\sqrt{3}}{4}d(1 + M) \tag{18}$$

$$x_{\text{CCD}} = \frac{d}{2}(1 + M). \tag{19}$$

Lastly, in KD, shift terms included to vertically fit an equilateral triangle into a rectangular CCD (last term of equations (4) and (5)) are no longer necessary, because the imaging volume is *defined* by the actual view of the CCDs instead of forcing a *predefined* imaging volume shape onto the CCDs. As seen in figures 9 and 13, such a predefinition results in incorrect ray tracing, which show that parts of the CCD never overlap. For this reason, the Z distance to the back of the imaging volume should always be set equal to L_{ft} so that the ray tracing correctly shows that the CCDs completely overlapped in that plane (see figure 15). This can easily be achieved by setting L_{ft} in equation (15) equal to the distance desired for the back of the imaging volume as given in equation (20):

$$L_{ft} = L_{apft} + a_z. \tag{20}$$

4. Geometric uncertainty analysis

A geometric uncertainty analysis is performed on the new rectangular definition for the imaging volume, using the method of Lawson and Wu (1997) as implemented by KD. In this approach, physical system parameters, such as lens focal length, lens separation side-length and distances to the CCDs and focal plane, are all assumed to have zero uncertainty in order to ascertain the uncertainty in a particle's position given the uncertainty of its image on the CCDs.

The equations for the X-direction remain the same as in KD (with the appropriate coordinate transform as from before), but the Y-direction equations are redefined from the new optical axis origin and with the lenses spaced equally $3\gamma/4$ above and below the axis, whereas in KD they were $\gamma/2$ and γ above and below, respectively (see figure 10). For comparison with KD, the entire set of uncertainty equations is shown in table 5. Equations (21)–(23) are the uncertainties in the physical location of the particle based on the particle image location on the CCD, the physical particle location and physical parameters of the imaging system.

As in KD, Δx is the uncertainty in measuring the particle image location on the CCD, where it is assumed that the uncertainties in all particle locations on the CCD are the

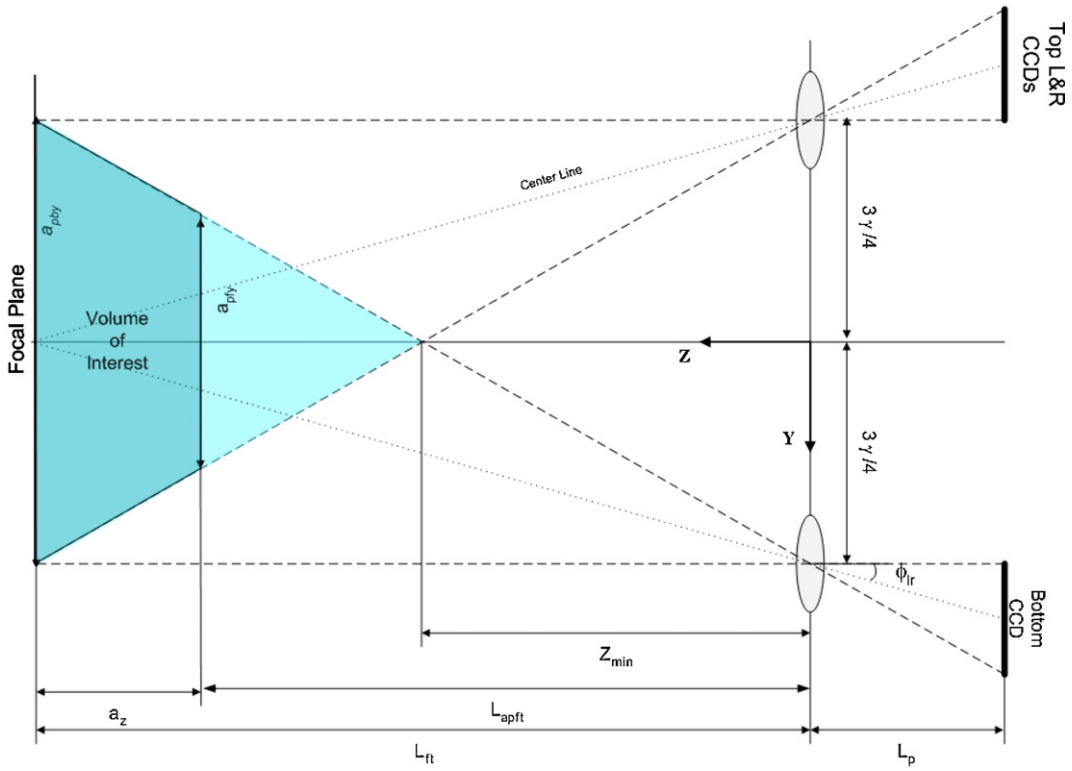

Figure 15. Rectangular imaging volume defined in the *Y*–*Z* plane. The back of the volume of interest has been shifted to the focal plane and is shown by the dark blue region, while the observable domain is identified by the combined light and dark blue region.

Table 5. Comparison between uncertainty equations in KD and present derivation.

	KD	Present derivation	Equation
$\delta(\mathrm{d}X)$	$\frac{(\Delta x)}{\sqrt{3}}\frac{\lvert Z\rvert}{MdL_{ft}}\sqrt{d^2+3X^2}$	$\frac{(\Delta x)}{\sqrt{3}}\frac{\lvert Z\rvert}{MdL_{ft}}\sqrt{d^2+3X^2}$	(21)
$\delta(\mathrm{d}Y)$	$\frac{(\Delta x)}{\sqrt{3}}\frac{\lvert Z\rvert}{MdL_{ft}}\sqrt{d^2+3Y^2}$	$\frac{(\Delta x)}{4\sqrt{3}}\frac{\lvert Z\rvert}{MdL_{ft}}\sqrt{17d^2+8\sqrt{3}Yd+48Y^2}$	(22)
$\delta(\mathrm{d}Z)$	$(\Delta x)\frac{Z^2}{MdL_{ft}}$	$(\Delta x)\frac{Z^2}{MdL_{ft}}$	(23)

same:

$$\delta(\mathrm{d}x_{tr}) = \delta(\mathrm{d}x_{tl}) = \delta(\mathrm{d}x_b) = \delta(\mathrm{d}y_{tr}) = \delta(\mathrm{d}y_{tl}) = \delta(\mathrm{d}x_b) = \Delta x. \quad (24)$$

As found throughout this paper, the *X*-direction equations are the same in this derivation as in KD, but the *Y*-direction equations differ. Taking a representative volume of interest (width of 100 mm) and camera physical parameters from Pereira and Gharib (2002) ($d = 100$ mm, $L_{ft} = 1000$ mm, $\Delta x = 0.025$, $h_1 = 10.24$ mm), the uncertainty in Y (from equation (22)) is plotted and compared in figure 16. An overall system error can be evaluated by integrating this error over Y/d at constant Z/d values. The bounds of integration defining this cross dimension are $-1/3 < Y/d < 2/3$ for KD, and $-1/2 < Y/d < 1/2$ for the present derivation. Performing this integration shows that the integrated error for the present derivation is 0.68% less in comparison with KD.

Similar to KD, out-of-plane to in-plane uncertainty ratios can also be derived, as they are good measures of the overall performance of the system. Table 6 shows these results in comparison with KD, where d is used as the non-dimensionalizing variable. Equations (25) and (26) are plotted in figures 17 and 18, with respect to X/d and Y/d, respectively.

Table 6. Comparison between error ratio equations in KD and present derivation.

	KD	Present derivation	Equation
$\frac{\delta(\mathrm{d}Z)}{\delta(\mathrm{d}X)}$	$\frac{\sqrt{3}(Z/d)}{\sqrt{1+3(X/d)^2}}$	$\frac{\sqrt{3}(Z/d)}{\sqrt{1+3(X/d)^2}}$	(25)
$\frac{\delta(\mathrm{d}Z)}{\delta(\mathrm{d}Y)}$	$\frac{\sqrt{3}(Z/d)}{\sqrt{1+3(Y/d)^2}}$	$\frac{4\sqrt{3}(Z/d)}{\sqrt{17+8\sqrt{3}(Y/d)+48(Y/d)^2}}$	(26)

The results are very similar to KD, with the error ratios responding linearly for changes in Z/d but having a peak that is off from the system optical axis. The error ratio versus X/d, figure 17, shows identical results to KD. Here, the error ratio falls off symmetrically about the system optical axis, with a maximum occurring on axis and minimums occurring as the particle moves farther outward. However, when plotted against Y/d, there is a noticeable shift in the peak of the error ratios. The shift in the peak is exactly $1/(4\sqrt{3})$, which is the non-

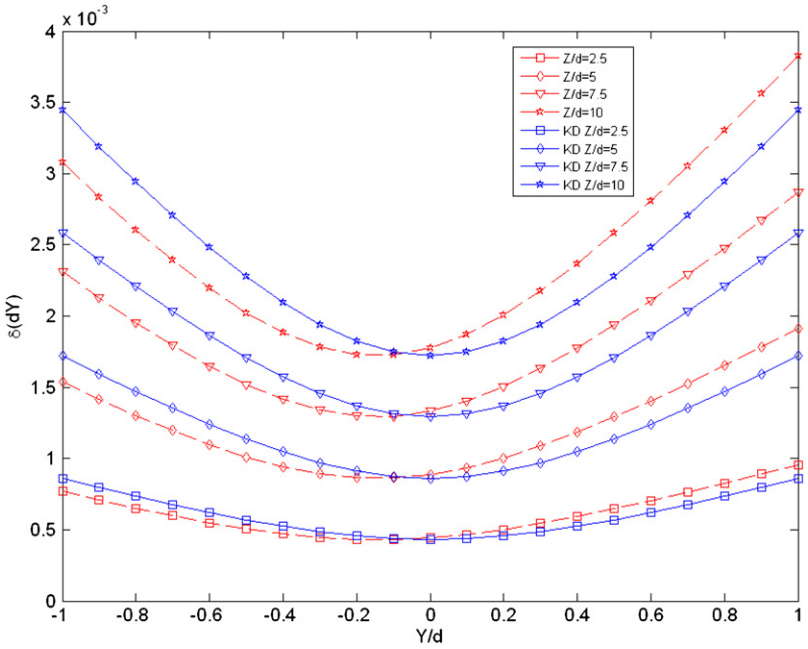

Figure 16. Absolute uncertainty $\delta(\mathrm{d}Y)$ comparison using a representative camera and imaging volume dimensions.

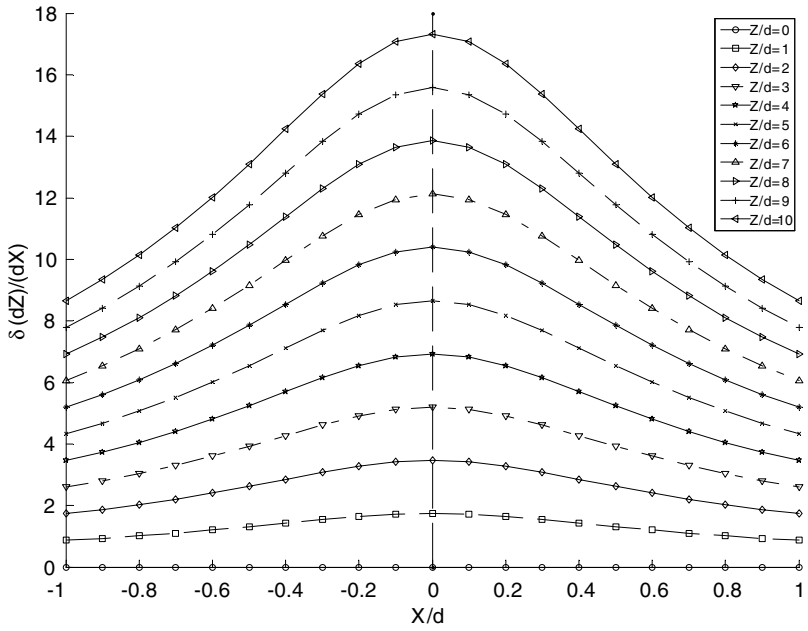

Figure 17. Error ratio $\frac{\delta(\mathrm{d}Z)}{\delta(\mathrm{d}X)}$ plotted for the physical off axis X/d locations with lines of constant Z/d, matching plot in KD

dimensionalized shift distance shown with the vertical dashed black line in figure 18 that corresponds to the shift required to move the system optical axis from the lens' equilateral triangle centroid to the half-height (see figure 10). This shows that the error distribution is centered on the lens' equilateral triangle centroid instead of the imaging volume location and that the shift of the optical axis is effectively moving the origin. Inserting $\frac{Y}{d} = \frac{Y}{d} - \frac{1}{4\sqrt{3}}$ into equation (26) confirms this as the original equation derived in KD. Because of the shift, the error ratios in the Y-direction are not symmetric about the system optical axis. Consequently, the error ratio for values to the left of $\frac{-1}{2(4\sqrt{3})}$ will have a higher value than KD, while the error ratio for values to the right of $\frac{-1}{2(4\sqrt{3})}$ will be lower. However, integrating over the cross-plane dimension ($-1/3 < Y/d < 2/3$ and $-1/2 < Y/d < 1/2$ for KD and the present derivation, respectively) for constant Z/d values gives an averaged error ratio that is larger for the present derivation with respect to

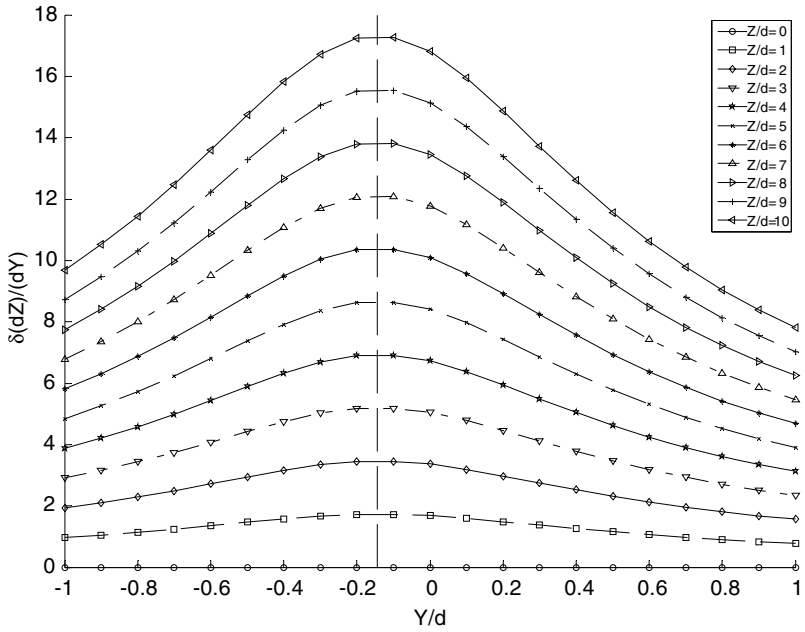

Figure 18. Error ratio $\frac{\delta(dZ)}{\delta(dY)}$ plotted for the physical off axis Y/d locations with lines of constant Z/d with peak shifted from KD.

KD by approximately 0.5%. This is a consequence of the fact that $\delta(dY)$ is less for the present derivation (see figure 16), indicating that the Y-direction has an increased overall error in KD in comparison to the present derivation.

5. Conclusions

Starting with the fully developed characterization of the defocused digital particle image velocimetry as presented by KD, this paper redefines the imaging volume from a predefined tetrahedral volume to a truncated rectangular pyramid, which more correctly characterizes how the CCDs are imaged. The equations were modified such that the coordinate system would match a conventional image coordinate system so that x is horizontal and positive to the right and y is vertical and positive down. Also, the equations for $Z_{\min}$ and d were modified to take into account the dimensions of the CCDs as opposed to KD where the sidelength of an equilateral triangle was used.

The equations to position the CCDs in space relative to the lenses, which were absent in KD, are presented here to complete the physical camera design and relate it directly to the imaged volume. The error analysis shows similar results to KD, with matching amplitudes and only a shift in the error ratio for the y-direction because of the now-symmetric spacing of the CCDs about the newly defined system optical axis, while maintaining an equilateral triangular shape for the lenses. The absolute error ratio integrated over a representative imaging volume, while holding Z/d constant is reduced from KD by approximately 0.68% by this new arrangement, whereas in the X-direction, the error remains the same for either arrangement.

This new definition of the imaging volume will allow a more exact and accurate characterization of the DDPIV system, as it correctly represents the physical volume imaged onto the CCD and its corresponding volume in space that is used for data collection. This will also allow the camera design process to specify a more practical and therefore useful imaging volume as an input, resulting in the parameters associated with its geometric configuration as outputs.

Acknowledgment

The authors gratefully acknowledge the support of the National Science Foundation (grant CTS-331140).

References

Barnheart D H, Adrian R J and Papen G C 1994 Phase-conjugate holographic system for high-resolution particle-image velocimetry *Appl. Opt.* **33** 7159–70

Kajitani L and Dabiri D 2005 A full three-dimensional characterization of defocusing digital particle image velocimetry *Meas. Sci. Technol.* **16** 790–804

Kajitani L and Dabiri D 2008 A full three-dimensional characterization of defocusing digital particle image velocimetry (Erratum) *Meas. Sci. Technol.* **19** 049801

Lawson N J and Wu J 1997 Three-dimensional particle image velocimetry: error analysis of stereoscopic techniques *Meas. Sci. Technol.* **8** 894–900

Maas H G, Gruen A and Papantoniou D 1993 Particle tracking velocimetry in three-dimensional flows *Exp. Fluids* **15** 133–46

Meng H and Hussain F 1995 In-line recording and off-axis viewing (IROV) technique for holographic particle velocimetry *Appl. Opt.* **34** 1827–40

Murai S, Nakamura H and Suzaki Y 1980 Analytical orientation for non-metric camera in the application to terrestrial photogrammetry *Int. Arch. Photogramm.* **23** 516–25

Pereira F and Gharib M 2002 Defocusing digital particle image velocimetry and the three-dimensional characterization of two-phase flows *Meas. Sci. Technol.* **13** 683–94

Pereira F, Gharib M, Dabiri D and Modarress D 2000 Defocusing digital particle image velocimetry. A 3-component 3-dimensional DPIV measurement technique: application to bubbly flows *Exp. Fluids* **29** S78–84

Ponchaut N F, Mouton C A and Hornung H G 2004 Development of three-dimensional particle tracking velocimetry for supersonic flow *AIAA Paper, 42nd AIAA Aerospace Sciences Meeting and Exhibit* pp 7822–31

Virant M and Dracos T 1997 3D PTV and its application on Lagrangian motion *Meas. Sci. Technol.* **8** 1539–52

Webster D R, Roberts P J W and Ra'ad L 2001 Simultaneous D P TV/PLIF measurements of a turbulent jet *Exp. Fluids* **30** 65–72

Willert C and Gharib M 1992 Three-dimensional particle imaging with a single camera *Exp. Fluids* **12** 353–8

Zhang J, Tao B and Katz J 1997 Turbulent flow measurement in a square duct with hybrid holographic PIV *Exp. Fluids* **23** 373–81

Zimin V, Meng H and Hussain F 1993 Innovative holographic particle velocimeter: a multibeam technique *Opt. Lett.* **18** 1101–3